

International Journal of Modern Physics D
 © World Scientific Publishing Company

Improved Simulation of the Mass Charging for ASTROD I

GANG BAO^{1,2,3}, WEI-TOU NI^{1,3}, D. N. A. SHAUL⁴, H. M. ARAUJO⁴, LEI LIU^{1,2}, T. J. SUMNER⁴

1. *Center for Gravitation and Cosmology, Purple Mountain Observatory, Chinese Academy of Sciences, Beijing West Road No.2, Nanjing, 210008, China*
2. *Graduate University of Chinese Academy of Sciences, Beijing, 100049, China*
bgastro@pmo.ac.cn
3. *National Astronomical Observatories, Chinese Academy of Sciences, Beijing, 100049, China*
4. *Department of Physics, Imperial College London, London, SW7 2BZ, UK*

Received Day Month Year
 Revised Day Month Year
 Communicated by

The electrostatic charging of the test mass in ASTROD I (Astrodynamical Space Test of Relativity using Optical Devices I) mission can affect the quality of the science data as a result of spurious Coulomb and Lorentz forces. To estimate the size of the resultant disturbances, credible predictions of charging rates and the charging noise are required. Using the GEANT4 software toolkit, we present a detailed Monte Carlo simulation of the ASTROD I test mass charging due to exposure of the spacecraft to galactic cosmic-ray (GCR) protons and alpha particles (³He, ⁴He) in the space environment. A positive charging rate of 33.3 e⁺/s at solar minimum is obtained. This figure reduces by 50% at solar maximum. Based on this charging rate and factoring in the contribution of minor cosmic-ray components, we calculate the acceleration noise and stiffness associated with charging. We conclude that the acceleration noise arising from Coulomb and Lorentz effects are well below the ASTROD I acceleration noise limit at 0.1 mHz both at solar minimum and maximum. The coherent Fourier components due to charging are investigated, it needs to be studied carefully in order to ensure that these do not compromise the quality of science data in the ASTROD I mission.

Keywords: ASTROD I; charging; GEANT4; disturbances.

1. Introduction

The ASTROD I (Astrodynamical Space Test of Relativity using Optical Devices I) mission concept is a down-scaled version of ASTROD. The main objectives of ASTROD I are: to improve the precision of measurement of solar-system dynamics, solar-system constants and ephemeris; to measure the relativistic gravitational effects; to test the fundamental laws of space-time more precisely and to improve the measurement of the rate of change of the gravitational constant with time.¹

The basic scheme of the ASTROD I space mission is to use two-way laser interferometric ranging and laser pulse ranging between a drag-free ASTROD I spacecraft in a solar orbit and deep space laser stations on Earth. The ASTROD I spacecraft

2 *G. BAO et al.*

is 3-axis stabilized with a total mass of 300-350 kg. The mass of the payload is 100-120 kg. The science data rate is 500 bps. The spacecraft is cylindrical with OD (Outer Diameter) 2.5 m and height 2 m and has its side surface covered with solar panels. In orbit, the cylindrical axis will be perpendicular to the orbit plane with the telescope pointing toward the ground laser station. The effective area to receive sunlight is about 5 m² and can generate over 500 W of power.¹⁻²

The spacecraft will be launched into the solar orbit from a low earth orbit. The injection correction will be made using a medium-sized ion thruster. A launch on August 4, 2010 would provide a suitable orbit. The orbit in the X-Y plane of the heliocentric ecliptic coordinate system is shown in Figure 1.^{1,3} This solar orbit will initially have a period of 290 days. After two gravity-assist encounters with Venus, the period will be shortened to about 165 days. After about 370 days from launch, the spacecraft will arrive at the other side of the Sun. The spacecraft will have the first closest approach to Venus 107.8 days after launch with a distance of 31606.0 km to the centre of Venus. The spacecraft crosses the Venus trajectory in front of Venus and gets a swing toward the Sun to achieve the Venus orbital period. After the first encounter, the spacecraft has the same orbit's period as Venus and encounters Venus again after about 1 period (224.7 days) with a closest approach distance of 16151.7 km from the centre of Venus.¹⁻²

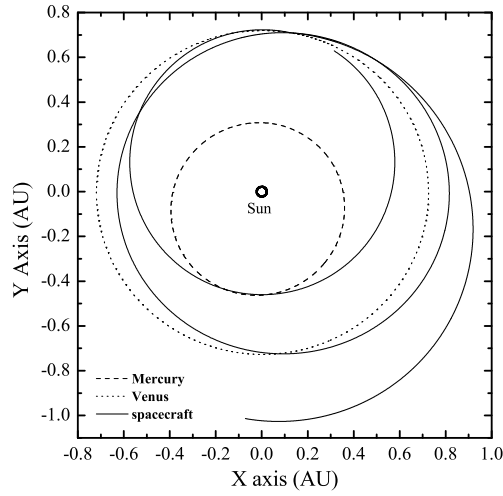


Fig. 1. The ASTROD I orbit in the X-Y plane of the heliocentric ecliptic coordinate system.

To achieve its goal, the ASTROD I residual acceleration noise target is:

$$S_{\Delta a}^{1/2}(f) = 3 \times 10^{-14} \left[\frac{0.3 \text{ mHz}}{f} + 30 \left(\frac{f}{3 \text{ mHz}} \right)^2 \right] \text{ ms}^{-2} \text{ Hz}^{-1/2}, \quad (1)$$

over the frequency range of $0.1 \text{ mHz} < f < 100 \text{ mHz}$.² Here $S_{\Delta a}^{1/2}(f)$ is the residual acceleration noise spectral density. It is compared to the LISA Pathfinder LISA

Technology Package,⁴ LISA⁵ and ASTROD⁶ noise target curves in Figure 2.

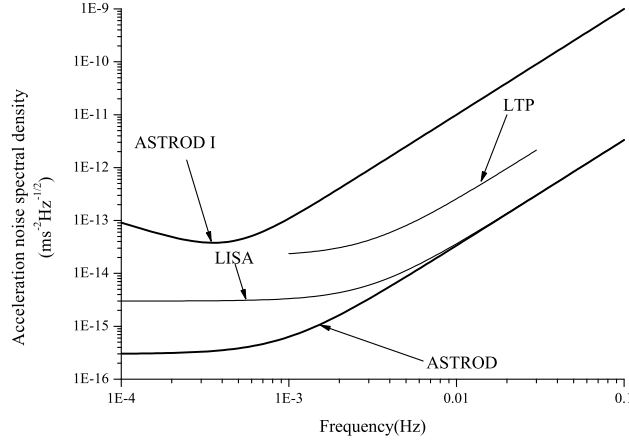


Fig. 2. A comparison of the target acceleration noise curves of ASTROD I, the LTP, LISA and ASTROD.

The test mass is key to guarantee the drag-free condition for ASTROD I. It is a 1.75 kg, rectangular parallelepiped, made of an extremely low magnetic susceptibility ($< 5 \times 10^{-5}$) Au-Pt alloy, to minimize magnetic disturbances. The test mass is placed in the centre of spacecraft and surrounded by electrodes on all six sides. Any relative displacement of test mass to the surrounding electrodes will be capacitively detected and the spacecraft will follow it using FEED (Field Emission Electric Propulsion) to ensure drag-free flight. Cosmic rays and solar energetic particles will easily penetrate the light shielding of the spacecraft to transfer heat, momentum and electrical charge to the test mass. Electrical charging is the most significant of these disturbances. It will result in forces on the test mass, due to Coulomb and Lorentz interactions, which will disturb the geodesic motion. The characteristics of the test mass charging process depend on the incident flux, spacecraft geometry and the physical processes that occur. The three main disturbances associated with this charge are an increase in the test mass acceleration noise, coupling between the test mass and the spacecraft and the appearance of coherent Fourier components in the measurement bandwidth.⁷ To limit the acceleration noise associated with Coulomb and Lorentz forces to meet the ASTROD I noise requirement, the test mass must be discharged in orbit. Our previous work predicted the charging rates for ASTROD I test mass from galactic cosmic rays at solar minimum using a simplified geometry, and using these predictions, estimated the magnitude of disturbances associated with charging.⁸ In this paper, we present the detailed calculation of the ASTROD I net test mass charging rate and shot noise, due to cosmic rays at solar minimum and solar maximum, with a more realistic geometry model. Based on these results, we estimate the magnitude of acceleration noise, stiffness and the coherent signals associated with charging.

2. Modelling the Charging Process

2.1. Radiation environment model

We have simulated the fluxes of the 3 most abundant primaries, proton, ^3He and ^4He primary particles which represent approximately 98% of the total cosmic ray flux. Near-Earth cosmic ray spectra were adopted, as used in similar LISA simulations. These are shown in Figure 3.⁹ The primary particles are generated from points

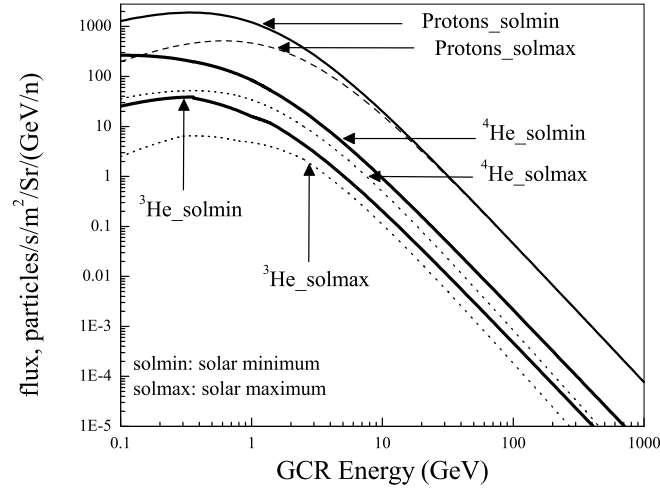


Fig. 3. Differential energy spectra for cosmic ray protons and He nuclei at near earth orbit. For each species, the upper curve indicates the solar minimum spectrum, the lower curve indicates the solar maximum spectrum.

sampled uniformly from a spherical surface of 3000 mm diameter, encompassing the whole ASTROD I geometry model.

The total time T for bombardment by N_0 primaries is given by $T = N_0 / F \cdot \pi R^2$, where F is the integral flux (unit: particles/cm²/s) for each species at solar minimum or solar maximum, and $R = 1500$ mm. The N^{th} particle event occurs at time $t = N \cdot T / N_0$.¹⁰ The effects on charging of other particle species (C, N, O, e⁻) are determined separately, based on a LISA study.¹¹ Work is under way to study the impact on the charging disturbances from variations in the incident flux due to the ASTROD I heliocentric position changes.

2.2. Physics model

Test mass charging depends heavily on the physics processes that occur during the passage of the particles through matter and the geometry model used in simulation. The GEANT4 toolkit employs Monte Carlo particle ray-tracing techniques to follow all primary and secondary particles. Due to their high energy and hadronic nature, cosmic rays can produce the complex nuclear reactions which have large

final-state multiplicities, producing many secondary particles. A low energy threshold of 250 eV was imposed for secondary particle production in our simulation. The physics processes simulated include electromagnetic, hadronic and photonuclear interactions. Fluorescence and non-radiative (Auger) atomic deexcitation have been implemented. The hadronic physics is mainly implemented by elastic and inelastic scattering processes. The inelastic reactions were based on the LEP (Low Energy Particles) and HEP (High Energy Particles) parameterized models. The inelastic reactions also use evaporation models to treat the deexcitation of nuclei with $A > 16$, comprising gamma emission, fragment evaporation (p, n, α , ^2H and ^3H) and fission of heavier residual nuclei. A variety of decay, capture and annihilation processes has also been included in our physics processes list based on LISA GEANT4 model of Araujo et al.¹² The charging potential of several additional physics processes, such as the kinetic emission of very low energy electrons which has not been modeled in the present simulation, has been assessed based on LISA studies.¹⁰

2.3. *Geometry model*

The basic payload configuration of ASTROD I is sketched in Ref. 1. The geometry model built for ASTROD I using GEANT4 in present work is sketched in Figure 4 and Figure 5. Table 1 lists the dimensions and weight of main constituent parts of the ASTROD I geometry model. Table 2 lists the composition and density of materials used in the model.

The cylindrical structure of the spacecraft consists of a layer with diameter 2.5 m, height 2 m and thickness 10 mm made of CFRP (Carbon Fibre Reinforced Plastic) honeycomb. The top and bottom of the spacecraft are covered by the upper deck and lower deck. To prevent sunlight from striking the inside directly and to reduce the temperature perturbation inside, all surfaces of spacecraft are covered by a thermal shield consistent of five layers of materials (face sheet, honey comb core, face sheet, foam, face sheet). The edges of upper deck and thermal shield are shown as large ellipses in Figure 4. The inner lower deck is shown as the grey part in Figure 4 and Figure 5. The payload structure is used for shielding the optical bench, inertial sensor and primary telescope etc. The primary telescope, which collects the incoming light is a 500 mm diameter f/1 Cassegrain telescope.¹³ Some 30 boxes represent the components above ~ 0.1 kg based on the payload configuration.¹ The mass of the spacecraft and payload are estimated as 341 kg and 109 kg in this study.

6 *G. BAO et al.*

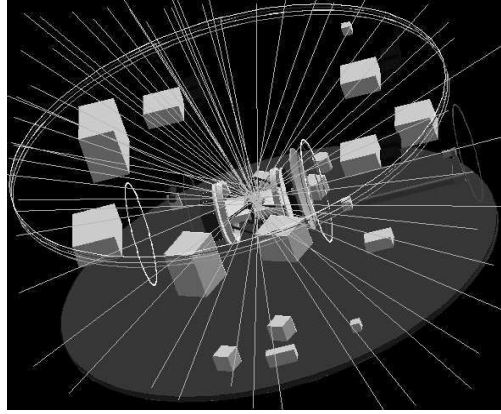


Fig. 4. The schematic diagram for the geometry model with a simulated GEANT4 cosmic-ray event.

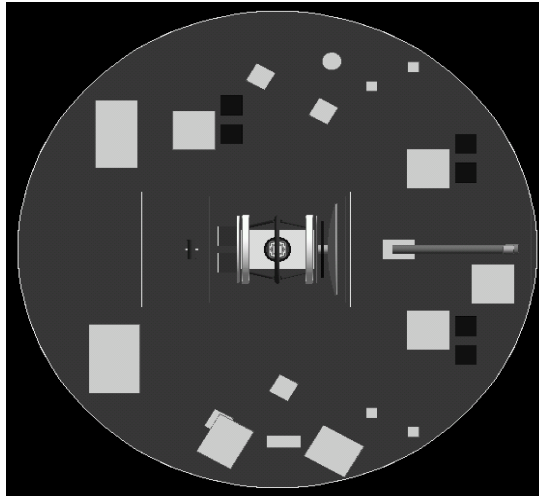


Fig. 5. The overhead view of the GEANT4 geometry model for ASTROD I. The six black boxes are laser heads and the other white boxes represent the components above ~ 0.1 kg.

Improved Simulation of the Mass Charging for ASTROD I 7

Table 1. Dimension and weight of the main constituent parts of the ASTROD I geometry model

Constituent part	Material	Weight (kg)	Dimension (mm)	Comment
Solar Panels	Scell	~61.5	Tube: radius 1250; height 2000; thickness 0.5	covers the side surface of the spacecraft
Spacecraft	CFRP	~7.8	Tube: radius 1250; height 2000; thickness 10	contains the payloads
Thermal Shield	CFRP Al-Honeycomb foam	~100.3	Tube: radius 1240; height 2000; thickness 41.8	covers the spacecraft
Upper Deck	CFRP Al-Honeycomb	~15	Cylinder: radius 1240; thickness 30	top of the spacecraft
Lower Deck	CFRP Al-Honeycomb	~15	Cylinder: radius 1240; thickness 30	above the MLI-blanket
MLI-blanket	MLImat	~6.8	Cylinder: radius 1240; thickness 1	bottom of the spacecraft
Payload Shield	CFRP	~15.6	Tube: radius 300; length 1000; thickness 5	Shields the optical bench, inertial sensor
Optical Bench	ULEglass	~5	Rectangular: length 350; width 200; height 40	contains the Ti-house
Ti House	Ti Alloy	~1.9	Tube: radius 62.5; height 224; thickness 5	located in the optical bench
Mo House	Molybdenum	~2.5	Cube: length 75	contains the test mass
Test Mass	AuPt Alloy	~1.75	Rectangular: length 50; width 50; height 35	
Primary Telescope	SiC	~6.4	Dish: radius 250; thickness 10.5	collects the incoming light
Shield/Mounting Plate	CFRP	~1.6	Cylinder: radius 175; thickness 10	
Telescope Shield	CFRP	~12.6	Tube: radius 285; length 860; thickness 5	Shields the secondary mirror
PCDU	Al6061	~15.9	Rectangular: length 350; width 200; height 300	Power Conditioning and Distribution Unit
Transponder	Al6061	~3.5	Rectangular: length 220; width 184; height 178	
CPS	Al6061	~15.9	Rectangular: length 240; width 356; height 140	Centralised Processor System
Interferometer Electronic Boxes	Al6061	~3.5	Rectangular: length 200; width 200; height 150	
Gyroscope	Al6061	~1	Cylinder: radius 42.5; height 89	
RFDU	Al6061	~1	Rectangular: length 160; width 60; height 80	Radio Frequency Distribution Unit

8 *G. BAO et al.*

Table 2. The composition and density of materials used in the ASTROD I geometry model (CFRP:Carbon Fibre Reinforced Plastic)

Material	Composition (by weight)	Density (g/cm ³)
Vacuum	gas	1.0×10^{-25}
Al6061	Al(98%), Mg(1%), Si(0.6%), Fe(0.4%)	2.70
Al Honeycomb	Al(98%), Mg(1%), Si(0.6%), Fe(0.4%)	0.05
MLImat	H(4.1958%), C(62.5017%), O(33.3025%)	1.40
Ti Alloy	Ti(90%), Al(6%), V(4%)	4.43
AuPt Alloy	Au(70%), Pt(30%)	19.92
ULE Glass	SiGlass(92.5%), TiGlass(7.5%)	2.21
foam	C(90%), H(10%)	0.05
SiGlass	O: 2, Si: 1	2.20
TiGlass	O: 2, Ti: 1	4.25
SHAPAL	Al: 2, N: 1	2.90
SiC	Si: 1, C: 1	3.10
Scell	Si	7.82
Molybdenum	Mo	10.22
Gold	Au	19.32
CFRP	C	1.66
carbon	C	2.10
CFRP Honeycomb	C	0.05

A $50 \times 50 \times 35$ mm³ test mass is at the centre of the spacecraft. The test mass is housed inside capacitance sensors located in optical bench mounted behind the telescope. The test mass is surrounded by sensing and actuation electrodes lodged in a molybdenum housing. A 0.3 μ m gold layer is plated on the entire inner surface of the sensor housing. The assembly is accommodated in a titanium vacuum (< 10 μ Pa) enclosure. The gap between test mass and electrodes along X axis or Y axis is 4 mm; that along Z axis is 2 mm.¹³ The GEANT4 model for inertial sensor is shown in Figure 6.

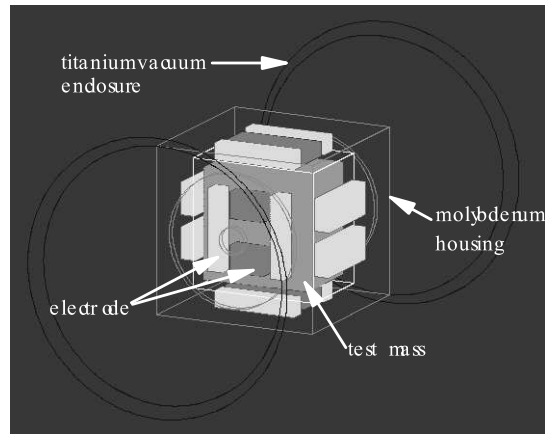


Fig. 6. ASTROD I inertial sensor model implemented in Geant4. The test mass, located at the centre of the figure, is surrounded by sensing electrodes (white) and injection electrodes (grey).

3. Charging Results

We have run 6 independent GEANT4 simulations to determine the charging of the ASTROD I test mass by cosmic ray protons, ^3He and ^4He , at solar minimum and maximum. In total, about 8,500,000 events were simulated. The details of each event that resulted in test mass charging were recorded, including the event time, net charge deposited on the test mass and the energy of the primary.

3.1. Charging simulation results

The variation of the net test mass charge with time, due to GCR proton, ^3He and ^4He fluxes are shown respectively in Figure 7, Figure 8 and Figure 9 at solar minimum and maximum. The straight lines in these figures correspond to least squares fits of the simulated data, giving mean net charging rates attributable to the proton, ^3He and ^4He fluxes. The proton flux is responsible for positive charging rates of $26.5 \pm 0.5 \text{ e}^+/\text{s}$ at solar minimum and $9.0 \pm 0.5 \text{ e}^+/\text{s}$ at solar maximum; The ^3He flux is responsible for positive charging rates of $0.8 \pm 0.05 \text{ e}^+/\text{s}$ at solar minimum and $0.3 \pm 0.05 \text{ e}^+/\text{s}$ at solar maximum; The ^4He flux is responsible for positive charging rates of $6.0 \pm 0.20 \text{ e}^+/\text{s}$ at solar minimum and $2.4 \pm 0.20 \text{ e}^+/\text{s}$ at solar maximum. The uncertainties quoted are only associated with the Monte Carlo fluctuations. Our simulation indicates that $\sim 97\%$ of the charge accumulated comes from primary cosmic ray protons and ^4He at both solar minimum and maximum and all three fluxes lead to positive charging of the test mass. The proton flux dominates these rates. However, ^4He , which constitutes only 8% of the total cosmic rays flux, is responsible for $\sim 18\%$ of the test mass charging at solar minimum and $\sim 20\%$ at solar maximum.

10 *G. BAO et al.*

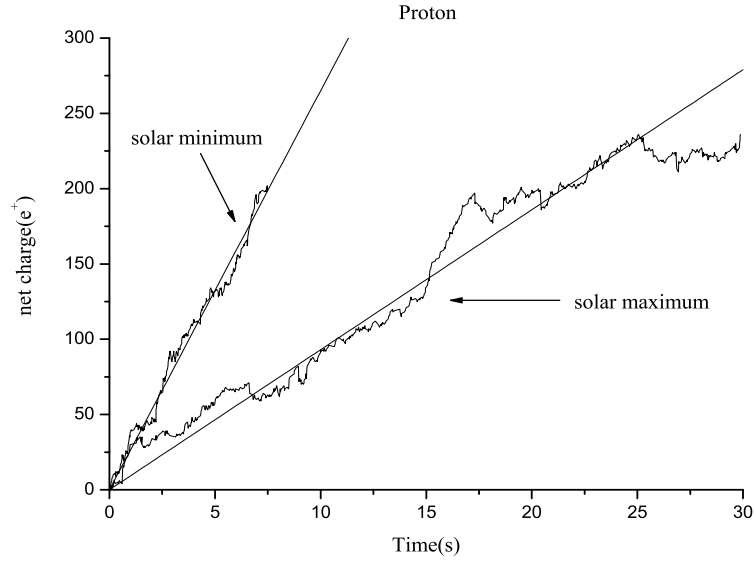


Fig. 7. The charging timeline for protons at solar minimum and maximum. The straight line is a least squares fit.

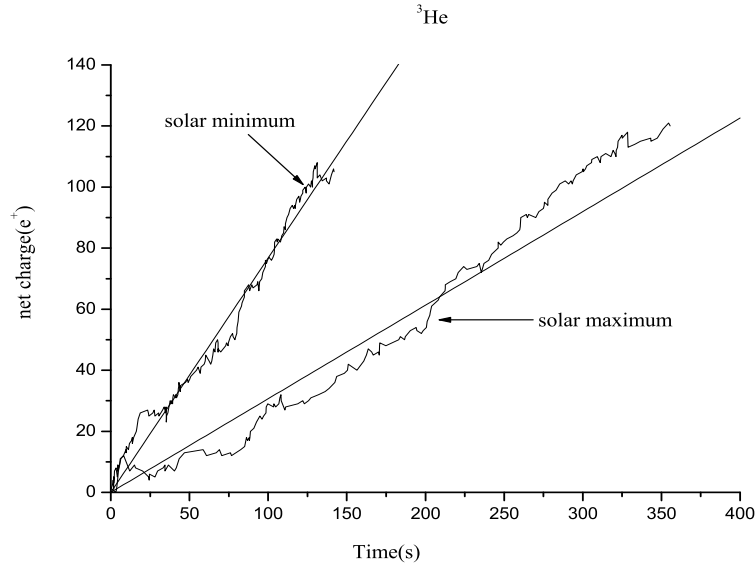


Fig. 8. The charging timeline for ^3He at solar minimum and maximum. The straight line is a least squares fit.

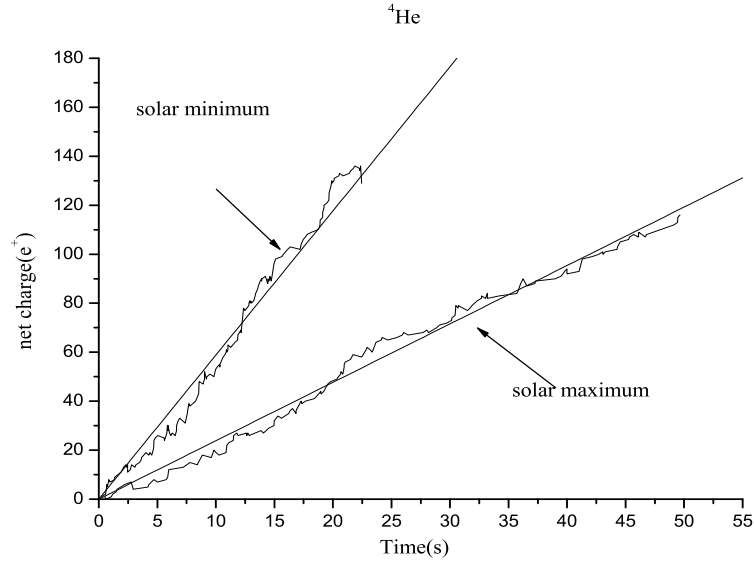
Improved Simulation of the Mass Charging for ASTROD I 11

Fig. 9. The charging timeline for ^4He at solar minimum and maximum. The straight line is a least squares fit.

Two histograms of the net charge deposited in an event are given in Figure 10 and Figure 11, for the proton data set, showing that most events result in the transfer of one unit of charge. The effects of the positive and negative chargings cancel to some extent. An imbalance in these currents gives rise to the net positive charging rate.

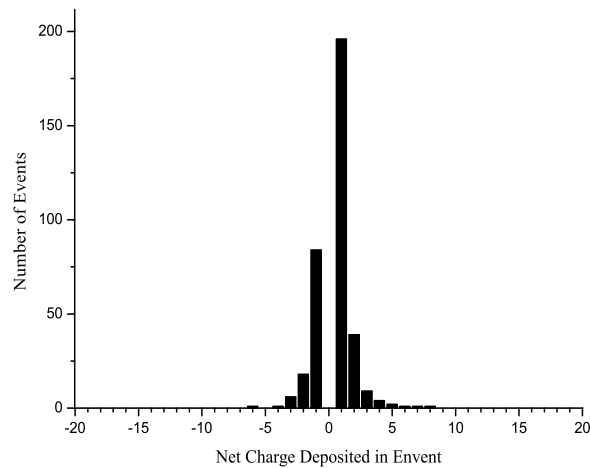


Fig. 10. Histogram of the net charge deposited in an event, for incident protons at solar minimum. The total number of proton events simulated was 2,290,000.

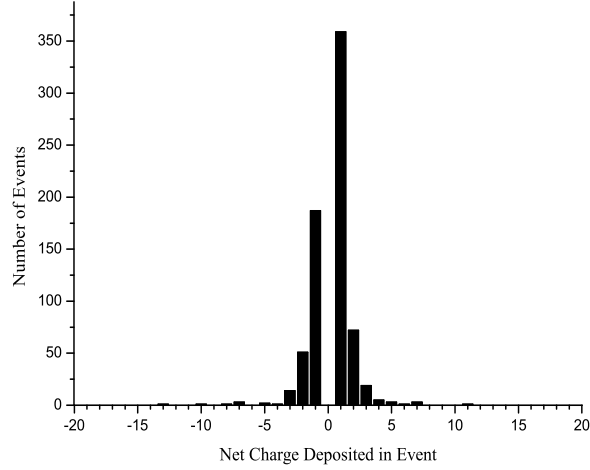
12 *G. BAO et al.*

Fig. 11. Histogram of the net charge deposited in an event, for incident protons at solar maximum. The total number of proton events simulated was 4,000,000.

The charging rate is plotted as a function of primary energy in Figure 12. The low energy cut-off is due to the shielding provided by the spacecraft, which prevents incident protons with energies below ~ 100 MeV from charging the test mass. At solar minimum, the most significant charging mechanism is primary cosmic ray particles stopping in the test mass. This occurs mainly for protons of energy between $\sim 100 - 720$ MeV. Protons with energies in excess of ~ 720 MeV have sufficient energy to traverse the distance through the spacecraft to the test mass and the longest path through the test mass, without being stopped. This explains the peak observed in this energy interval in Figure 12 at solar minimum. The scenario at solar maximum is distinct: a peak is visible at higher energies because the primary proton flux peak shifts towards higher energy.

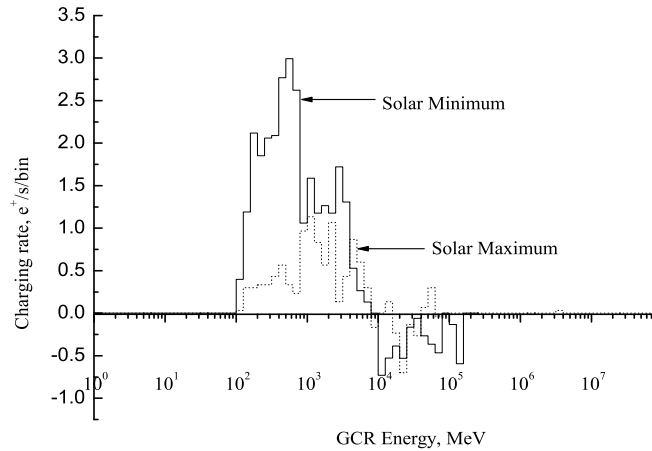


Fig. 12. Charging rate of test mass as a function of primary proton energy at solar minimum and at solar maximum.

In addition to the Monte Carlo uncertainty, we added an error of $\pm 30\%$ in the net charging rates to account for uncertainties in the GCR spectra, physics models and geometry implementation. Further, based on LISA studies^{10,11}, a potential contribution to the charging rate of $28.4 \text{ e}^+/\text{s}$ at solar minimum and of $17.0 \text{ e}^+/\text{s}$ at solar maximum from kinetic low energy secondary electron emission should be considered; the effect of cosmic ray fluxes of particle species not included in this simulation is expected to increase the net charging rate by $\sim 4.2\%$ at solar minimum and $\sim 7.3\%$ at solar maximum¹³.

3.2. Charging noise

Following to Ref. 12, the charging flux is considered to be made up of independent currents, I_q , each composed solely of charges qe ($q=+1$ for protons), with shot noise of single-sided spectral density $S_q = \sqrt{2qeI_q}$, where e is the magnitude of electron charge. The total noise, S_R , is then given by the quadrature sum of S_q , over all values of q . Considering the Monte Carlo currents alone, $S_q = 17.6 \text{ es}^{-1}\text{Hz}^{-1/2}$ at solar minimum and $S_q = 9.6 \text{ es}^{-1}\text{Hz}^{-1/2}$ at solar maximum. Based on the LISA study¹⁰, low energy secondary electron emission is estimated to contribute an extra $10.3 \text{ es}^{-1}\text{Hz}^{-1/2}$ at solar minimum and $8.0 \text{ es}^{-1}\text{Hz}^{-1/2}$ at solar maximum; the charging noises from other species (C, N, O, e^-) are estimated to be $8.9 \text{ es}^{-1}\text{Hz}^{-1/2}$ at solar minimum and $3.7 \text{ es}^{-1}\text{Hz}^{-1/2}$ at solar maximum. Integrating in the time domain gives the charging fluctuations at frequency f ,

$$S_Q(f) = S_R/2\pi f. \quad (2)$$

The charging rate and noise contributions from the different sources mentioned above are summarized in Table 3. Given the results in Table 3, by adding the contributions of all the independent sources, we estimate the total worst case charging rate to be $73.8 \text{ e}^+/\text{s}$ at solar minimum and $33.8 \text{ e}^+/\text{s}$ at solar maximum. The total worst case noise is $22.3 \text{ es}^{-1}\text{Hz}^{-1/2}$ at solar minimum and $13.0 \text{ es}^{-1}\text{Hz}^{-1/2}$ at solar maximum.

Table 3. The charging rate and noise contributions from different sources.

Source	charging rate(e^+/s)		charging noise($\text{e}/\text{s}/\text{Hz}^{1/2}$)	
	min	max	min	max
p	26.5	9.0	15.9	8.6
^3He	0.8	0.3	2.5	1.6
^4He	6.0	2.4	7.2	3.9
Secondary Electron	28.4	17.0	10.3	8.0
Other Species(C, N, O, e^-)	1.4	0.9	8.9	3.7
Uncertainty	10.0	3.5	-	-

4. Acceleration Disturbances

4.1. Coulomb noise and stiffness

The charge-dependent Coulomb acceleration a_{QK} in direction \hat{k} is given by:

$$a_{QK} = \frac{Q^2}{2mC_T^2} \frac{\partial C_T}{\partial k} + \frac{QV_T}{mC_T} \frac{\partial C_T}{\partial k} - \frac{Q}{mC_T} \sum_{i=1}^{N-1} V_i \frac{\partial C_{i,N}}{\partial k}. \quad (3)$$

The first two terms in equation (3) are dependent on the overall sensor geometric symmetry, through $\partial C_T / \partial k$, and the third term is dependent on the symmetry of the sensor voltage distribution. The corresponding acceleration noise, δa_{Qk} , due to random fluctuations of the test mass position relative to the spacecraft, δk , of the potentials of the conductors that surround the test mass, δV_i , and of the test mass free charge δQ , is given by:

$$\delta a_{QK}^2 = \left(\frac{\partial a_{QK}}{\partial k} \right)^2 \delta k^2 + \sum_{i=1}^{N-1} \left(\frac{\partial a_{QK}}{\partial V_i} \right)^2 \delta V_i^2 + \left(\frac{\partial a_{QK}}{\partial Q} \right)^2 \delta Q^2 \quad (4)$$

where k is a displacement in direction \hat{k} ; m is the mass of the test mass; Q is the free charge accumulated on the test mass; $C_{i,j}$ is the capacitance between conductors i and j which surround the test mass; V_i is the potential to which conductor i is raised; $C_T \equiv \sum_{i=1}^{N-1} C_{i,N}$ is the coefficient of capacitance of the test mass, which is defined as the N^{th} conductor, with potential $V_N = Q/C_T + V_T$, and $V_T \equiv \frac{1}{C_T} \sum_{i=1}^{N-1} C_{i,N} \cdot V_i$.⁷ The estimates for acceleration noise have assumed typical parameter values for the ASTROD I mission: Q was taken as the amount of charge accumulated in 1 day, assuming a net test mass charging rate of $73.8 \text{ e}^+/\text{s}$ at solar minimum and $33.8 \text{ e}^+/\text{s}$ at solar maximum, which corresponds to the Monte Carlo rate, with error margins, estimated contributions from particle species not included in the Monte Carlo model and the potential contribution from kinetic low energy secondary electron emission, that is likely to almost cancel in the actual sensor,¹⁰ added; $m = 1.75 \text{ kg}$; mean voltages on opposing conductors $V_i = 0.5 \text{ V}$; the potential difference between conductors on opposing faces of the sensor compensated to 10 mV ; the asymmetry in gap across opposite sides of test mass is $10 \text{ }\mu\text{m}$; capacitances and capacitance gradients were calculated using parallel plate approximations: $C_T = 53 \text{ pF}$; $V_T = 0.5 \text{ V}$; position noise $\delta k = 1 \times 10^{-7} \text{ mHz}^{-1/2}$; voltage noise $\delta V_i = 1 \times 10^{-4} \text{ VHz}^{-1/2}$ and charge noise $\delta Q = 4.6 \times 10^{-15} \text{ CHz}^{-1/2}$, which includes, as for the charging rate, the unmodelled contributions. These Coulomb acceleration noise due to the test mass charging are listed in Table 4. The total noise estimated here is a factor of ~ 30 less than the ASTROD I acceleration noise target. The stiffness associated with test mass charging, S_{Qk} , is given by $S_{Qk} = -m \cdot \partial a_{Qk} / \partial k$. These acceleration noise figures are lower than the results liberally estimated by Shiomi and Ni¹⁴ because of the smaller charging rate and charging noise we obtained here. The requirements on Coulomb noise, stiffness and other associated noises for ASTROD I in Ref. 14 are satisfied.

Table 4. The magnitude of charging disturbances for ASTROD I at solar minimum and maximum, at frequency = 0.1 mHz.

Solar activity	Coulomb noise ($\times 10^{-15} \text{ms}^{-2} \text{Hz}^{-0.5}$)				Lorentz noise ($\times 10^{-15} \text{ms}^{-2} \text{Hz}^{-0.5}$)	Stiffness ($\times 10^{-8} \text{s}^{-2}$)
	δk	δV_i	δQ	total		
minimum	1.06	2.18	1.32	2.80	2.80	-1.52
maximum	0.49	1.08	0.77	1.40	1.30	-0.69

δk : displacement noise; δV_i : voltage noise; δQ : charge noise.

4.2. Lorentz noise

Lorentz effects arise from the motion of the test mass through the interplanetary magnetic field, \vec{B}_I and its residual motion through the field generated within the spacecraft, \vec{B}_S . The test mass will be housed in a conducting enclosure, which will reduce the effect of the interplanetary field, via the Hall effect, with efficiency η . Hence, to first order, the Lorentz acceleration noise, a_L , is given by:

$$m^2(a_L)^2 = (\eta Q V_I \delta B_I)^2 + (\eta Q \delta V_I B_I)^2 + (Q \delta V_S B_S)^2 + (\eta \delta Q V_I B_I)^2. \quad (5)$$

where V_I is the speed of the test mass through the interplanetary field; δV_I and δV_S are the magnitudes of random fluctuations in the test mass velocity through the interplanetary field and relative to the spacecraft, respectively and δB_I gives the magnitude of fluctuations in the interplanetary field.⁷ a_L also increases with decreasing frequency, and is estimated to be $\sim 2.8 \times 10^{-15} \text{ms}^{-2} \text{Hz}^{-1/2}$ (0.1 mHz) at solar minimum and $\sim 1.3 \times 10^{-15} \text{ms}^{-2} \text{Hz}^{-1/2}$ (0.1 mHz) at solar maximum, which is a factor of ~ 30 below the ASTROD I acceleration noise target. We have assumed that $Q = 73.8 \text{e}^+/\text{s}$ at solar minimum and $33.8 \text{e}^+/\text{s}$ at solar maximum, as in section 4.1; $\eta = 0.1$; $\vec{V}_I = 4 \times 10^4 \text{m/s}$; $\delta V_I = 4.78 \times 10^{-12} \text{ms}^{-1} \text{Hz}^{-1/2}$; $\delta V_S = 6.28 \times 10^{-11} \text{ms}^{-1} \text{Hz}^{-1/2}$; $\vec{B}_S = 9.6 \times 10^{-6} \text{T}$; $|\delta B_S| = 1 \times 10^{-7} \text{THz}^{-1/2}$; $\vec{B}_I = 1.2 \times 10^{-7} \text{T}$ (this is a conservative estimate of the field at 0.5 AU, used to give the worst-case noise, for the ASTROD I orbit) and $|\delta B_I| = 1.2 \times 10^{-6} \text{THz}^{-1/2}$. The estimates of acceleration noises and stiffness due to the Coulomb and Lorentz effects are listed in Table 4.

4.3. Coherent Fourier components

The charging of the test mass may also result in the appearance of unwanted, coherent Fourier components in the ASTROD I measurement bandwidth through Coulomb and Lorentz interactions, due to the time dependence of the amount of charge accumulated on the test mass. It is shown that the signals associated with Lorentz interactions are expected to fall below the ASTROD I test mass residual acceleration noise, but the signals from Coulomb interactions may exceed both the instrumental noise over a fraction of the bandwidth, and may not be eliminated by

daily discharging of the test mass. The free charge on the test mass at time t can be expressed as follows:

$$Q(t) \approx \bar{Q}t. \quad (6)$$

where t is the time for which the test mass has been allowed to charge and \bar{Q} is the mean charging rate. Here, \bar{Q} is assumed to be constant. Substituting $Q(t) \approx \bar{Q}t$ into the expressions for the Coulomb and the Lorentz accelerations gives the terms¹⁵:

$$f_k(t) \equiv \Xi_k t^2 \equiv \frac{\bar{Q}^2}{2mC_T^2} \frac{\partial C_T}{\partial k} t^2, \quad (7)$$

$$e_k(t) \equiv \Theta_k t \equiv -\frac{\partial V_T}{\partial k} \frac{\bar{Q}}{m} t, \quad (8)$$

$$l_k(t) \equiv \Phi_k t \equiv \frac{\eta \bar{Q} t}{m} (\vec{V}_I \times \vec{B}_I) \cdot \hat{k}, \quad (9)$$

where $f_k(t)$ is dependent on the overall sensor geometric symmetry; $e_k(t)$ is dependent on the symmetry of the sensor voltage distribution; $l_k(t)$ is caused by the interplanetary magnetic field. The Fourier transforms of these signals with fixed-interval discharge will be described by a series of sinc functions ($\text{sinc}(x) = \sin \pi x / \pi x$). The equivalent one-sided power spectral density for these coherent signals is given by $P_{FT}^2 = 2FT^2/\tau$, where FT = Fourier transform of the signal and τ is the length of the data sample time.

Implementing the parameter values given in section 4.1 and 4.2, taking the mean charging rate as constant and assuming that the test mass is discharged once every 24 hours (as described in Ref. 15), the spectral densities of $f_k(t)$, $e_k(t)$ and $l_k(t)$ are estimated. The curves in figure 13 and figure 14 trace $P_{F_k(f)}$, $P_{E_k(f)}$ and $P_{L_k(f)}$, at the primary peaks of the sinc functions, where $F_k(f)$, $E_k(f)$ and $L_k(f)$ are the Fourier transform of $f_k(t)$, $e_k(t)$ and $l_k(t)$. $f_k(t)$ and $e_k(t)$ exceed the ASTROD I acceleration noise limit of $3 \times 10^{-14} [0.3 \text{ mHz}/f + 30(f/3 \text{ mHz})^2] \text{ ms}^{-2} \text{ Hz}^{-1/2}$ in a fraction of frequency bins in the frequency range of $0.1 \text{ mHz} < f < 4 \text{ mHz}$ at solar minimum (see Figure 13); only $e_k(t)$ exceeds the limit in a fraction of frequency bins in the frequency range of $0.1 \text{ mHz} < f < 2 \text{ mHz}$ at solar maximum (see Figure 14). These effects are more severe as frequency decreases. Several schemes could be used to minimize a potential loss of the ASTROD I science data, including continuously discharging the test mass, minimizing sensor voltage and geometrical offsets and through spectral analysis.¹⁵

Variations in, for example, the mean charging rate, could result in these signals exceeding the noise target in a larger fraction of the bandwidth. Hence, variations in these signals need to be studied carefully as they will influence the accuracy with which the solar-system and relativistic parameters can be determined.

A charge management system has been developed by Imperial College London, for LISA Pathfinder. This system has been extensively tested, both via simulations and laboratory tests.^{16–18} A similar system could easily be used for ASTROD I.

Improved Simulation of the Mass Charging for ASTROD I 17

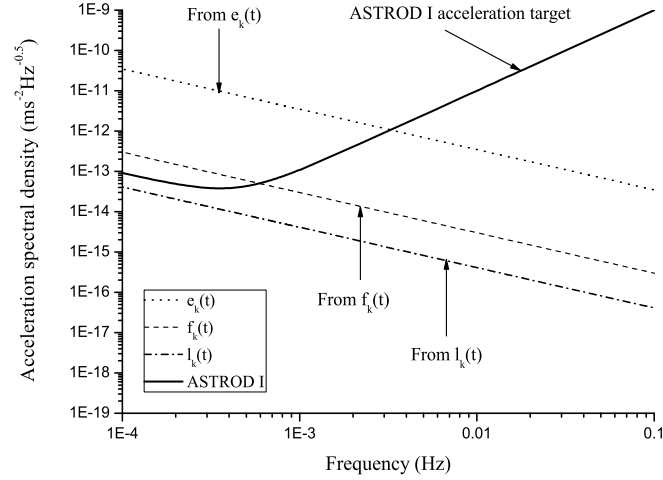


Fig. 13. The curves trace the spectral densities at the primary peaks of the sinc functions at solar minimum, of the coherent Fourier components, for $\tau=1$ year: $e_k(t)$ is given by the dotted line, $f_k(t)$ is given by the dashed line and $l_k(t)$ is given by the dashed-dotted line. The bold full line gives the ASTROD I acceleration noise limit.

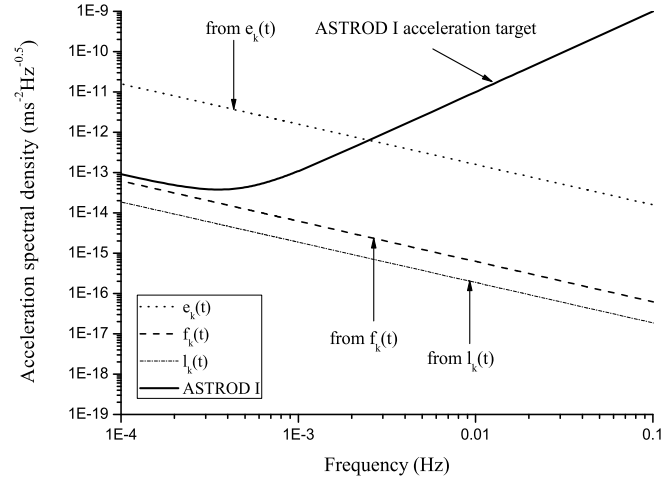


Fig. 14. The curves trace the spectral densities at the primary peaks of the sinc functions at solar maximum, of the coherent Fourier components, for $\tau=1$ year: $e_k(t)$ is given by the dotted line, $f_k(t)$ is given by the dashed line and $l_k(t)$ is given by the dashed-dotted line. The bold full line gives the ASTROD I acceleration noise limit.

5. Conclusion

The charging of the ASTROD I test mass by cosmic ray protons and alpha particles (^3He and ^4He) has been simulated using the GEANT4 toolkit at solar minimum

and maximum. The Monte Carlo model predicted a net charging rate of ~ 11.7 e^+/s at solar maximum, rising to 33.3 e^+/s at solar minimum. Although the proton flux is the dominant charging flux, ^4He , which constitutes only 8% of the total cosmic ray flux, is responsible for $\sim 18\%$ and $\sim 20\%$ of this rate at solar minimum and maximum, respectively. We have also included an additional net charging rate contribution due to particle species that were not included in the Monte Carlo model, and a potential charging mechanism, due to kinetic low energy secondary electron emission based on LISA studies.^{10,11} There is an additional uncertainty of $\pm 30\%$ in the net charging rate, due to uncertainties in the cosmic ray spectra, physics models and geometry implementation. A recent, preliminary, comparison of a simplified GEANT4 simulation and actual GP-B charging rates, indicate 45% agreement (GP-B simulation is larger than experimental value by 45%), reinforcing confidence in these predictions.^{18,19}

The ASTROD I acceleration noise limit is $10^{-13} \text{ ms}^{-2}\text{Hz}^{-1/2}$ at 0.1 mHz, which is less stringent than the LISA requirement. The magnitudes of the Coulomb and Lorentz acceleration noise associated with test mass charging increase with decreasing frequency. At the lowest frequency in the ASTROD I bandwidth, 0.1 mHz, the estimates of the Coulomb and Lorentz acceleration noise are both well below the acceleration noise target. These results agree, to within 30%, with those from our earlier study⁸, which was based on a simple geometry model. The variations in the test mass charging rate will alter the spectral description of the coherent Fourier components. Hence, further work is needed to ensure that these do not compromise the quality of the science data of the ASTROD I mission.

The charging process of the ASTROD I test mass by SEPs (Solar Energetic Particles) has also been simulated using the GEANT4 toolkit, and the charging rate is much larger than the values due to GCR (Galactic Cosmic Ray) proton flux at solar maximum and solar minimum.^{20–22} However, the charge management hardware described in reference 18 could be used to discharge a test mass even during solar events, provided safe operation could be ensured.

The effect of cosmic ray fluxes of particle species not included in the Monte Carlo simulation needs to be verified for the ASTROD I geometry. According to the recent work by Grimani et al.,²¹ the charging rate in each LISA test mass induced by primary and interplanetary electrons is comparable (absolute value) to that released by the nuclei of the C, N, O group at solar minimum. The acceleration disturbances due to charging of the ASTROD I test mass by electrons are also under study. Further, we will evaluate the variation in the ASTROD I test mass charging rate over the orbit over the solar cycle, including a detailed study of SEP events, and its variation due to modulation of cosmic ray flux over the ASTROD I orbit. For this, a SCoRE (Solar And Cosmic Ray Physics And The Space Environment: Studies For And With LISA) study along the line of Shaul et al.²² would be useful.

Acknowledgments

This work is funded by the National Natural Science Foundation (Grant Nos 10475114 and 10573037) and the Foundation of Minor Planets of Purple Mountain Observatory.

References

1. W.-T. Ni, Y. Bao, H. Dittus, T. Huang, C. Lammerzähl, G. Li, J. Luo, Z.-G. Ma, J.F. Mangin, Y.-X. Nie, A. Peters, A. Rudiger, E. Samain, S. Shiomi, T. Sumner, C.-J. Tang, J. Tao, P. Touboul, H. Wang, A. Wicht, X.-J. Wu, Y. Xiong, C. Xu, J. Yan, D.-Z. Yao, H.-C. Yeh, S.-L. Zhang, Y.-Z. Zhang, Z.-B. Zhou.: ASTROD I: Mission Concept and Venus Flybys, *Proc. 5th IAA Intl Conf. On Low-Cost Planetary Missions*, ESTEC, Noordwijk, The Netherlands, 24-26 September 2003, ESA SP-542, November 2003, pp.79-86; *ibid.*, *Acta Astronautica* **59**, 598 (2006)
2. W.-T. Ni, H. Araujo, G. Bao, H. Dittus, T.-Y. Huang, S. Klioner, S. Kopeikin, G. Krasinsky, C. Lammerzähl, G.-Y. Li, H.-Y. Li, L. Liu, Y.-X. Nie, A. Paton, A. Peters, E. Pitjeva, A. Rudiger, E. Samain, D. Shaul, S. Schiller, J.-C. Shi, S. Shiomi, M.H. Soffel, T. Sumner, S. Theil, P. Touboul, P. Vrancken, F. Wang, H.-T Wang, Z.-Y. Wei, A. Wicht, X.-J. Wu, Y. Xia, Y.-H. Xiong, C.-M. Xu, J. Yan, H.-C. Yeh, Y.-Z. Zhang, C. Zhao, and Z.-B. Zhou, *Journal of Physics: Conference Series*, **32**, 154 (2006).
3. C.-J. Tang, C.-H. Chang, W.-T. Ni, A.-M. Wu, *Orbit Design for ASTROD I*, 2003 report.
4. S. Vitale, P. Bender, A. Brillet, S. Buchman, A. Cavalleri, M. Cerdonio, M. Cruise, C. Cutler, K. Danzmann, R. Dolesi, W. Folkner, A. Gianolio, Y. Jafry, Gunther. Hasinger, G. Heinzel, C. Hogan, M. Hueller, J. Hough, S. Phinney, T. Prince, D. Richstone, D. Robertson, M. Rodrigues, A. Rudiger, M. Sandford, R. Schilling, D. Shoemaker, B. Schutz, R. Stebbins, C. Stubbs, T. Sumner, K. Thorne, M. Tinto, P. Touboul, H. Ward, W. Weber, W. Winkler, *Nucl. Phys. B (Proc. Suppl.)*, **110**, 209 (2002).
5. P. L. Bender, et al. *LISA Pre-Phase A Report 2nd edn MPQ233* (1998).
6. W.-T. Ni, ASTROD (Astrodynamical Space Test of Relativity using Optical Devices) and ASTROD I, *Nucl. Phys. B (Proc. Suppl.)*, **166**, 153 (2007).
7. D. Shaul, H. Araujo, G. Rochester, T. Sumner, P. Wass, *Class. Quantum Grav.*, **22**, 297 (2005).
8. G. Bao, D. Shaul, H. Araujo, W.-T. Ni, T. Sumner, L. Liu, *General Relativity and Gravitation*, **39**, No. 00, 000 (2007); arXiv: 0704.3303v1.
9. C. Grimaldi, H. Vocca, M. Barone, R. Stanga, F. Vetrano, A. Vicere, P. Amico, L. Bosi, F. Marchesoni, M. Punturo, and F. Travasso, *Class. Quantum Grav.*, **21**, S629 (2004).
10. H. Araujo, P. Wass, D. Shaul, G. Rochester, T. Sumner, *Astroparticle Physics*, **22**, 451 (2005).
11. C. Grimaldi, H. Vocca, G. Bagni, L. Marconi, R. Stanga, F. Vetrano, A. Vicere, P. Amico, L. Gammaitoni, and F. Marchesoni, *Class. Quantum Grav.*, **22**, S327 (2005).
12. H. Araujo, A. Howard, D. Shaul, and T. Sumner, *Class. Quantum Grav.*, **20**, S311 (2003).
13. G. Bao, L. Liu, D. Shaul, H. Araujo, W.-T. Ni, and T. Sumner, *Nucl. Phys. B (Proc. Suppl.)*, **166**, 246 (2007).
14. S. Shiomi and W.-T. Ni, *Class. Quantum Grav.*, **23**, 1 (2006).
15. D. Shaul, T. Sumner, G. Rochester, *International Journal of Modern Physics D*, **14**, 51 (2005).
16. M. Schulte, G. Rochester, D. Shaul, T. Sumner, C. Trenkel and P. Wass, AIP Confer-

- ence Proceeding–November 29, 2006–Volume 873, *Laser Interferometer Space Antenna 6th International LISA Symposium*, edited by S. M. Merkowitz and J. C. Livas, 165-171 (2006).
17. P. Wass, L. Carbone, A. Cavalleri, G. Ciani, R. Dolesi, M. Hueller, G. Rochester, M. Schulte, T. Sumner, D. Tombolato, C. Trenkel, S. Vitale, and W. Weber, AIP Conference Proceeding–November 29, 2006–Volume 873, *Laser Interferometer Space Antenna 6th International LISA Symposium*, edited by S. M. Merkowitz and J. C. Livas, 220-224 (2006).
 18. D. Shaul, Charge Management for LISA and LISA Pathfinder, *IJMPD*, this issue.
 19. J.P. Turneaure et al., *Advances in Space Research*, **32**, 1387 (2003).
 20. L. Liu, G. Bao, W.-T. Ni and D. Shaul, Simulation of ASTROD I test mass charging due to solar energetic particles, submitted to *Adv. Space Res.*, November, 2006; arXiv:0704.3493v1.
 21. C. Grimani, M. Fabi, R. Stanga, and L. Marconi, AIP Conference Proceeding–November 29, 2006–Volume 873, *Laser Interferometer Space Antenna 6th International LISA Symposium*, edited by S. M. Merkowitz and J. C. Livas, 184-188 (2006).
 22. D. Shaul, K. Aplin, H. Araujo, R. Bingham, J. Blake, G. Branduardi-Raymont, S. Buchman, A. Fazakerley, L. Finn, L. Fletcher, A. Glover, C. Grimani, M. Hapgood, B. Kellet, S. Matthews, T. Mulligan, W.-T. Ni, P. Nieminen, A. Posner, J. Quenby, P. Roming, H. Spence, T. Sumner, H. Vocca, P. Wass and P. Young, AIP Conference Proceeding–November 29, 2006–Volume 873, *Laser Interferometer Space Antenna 6th International LISA Symposium*, edited by S. M. Merkowitz and J. C. Livas, 172-178 (2006).